Reconstructing Ocean Surface Current Combining Altimetry and Future Spaceborne Doppler Data

Clement Ubelmann[1], Gérald Dibarboure[2], Lucile Gaultier[3], Aurélien Ponte[4], Fabrice Ardhuin[4], Maxime Ballarotta[5]and Yannice Faugère[5]

[1]Ocean Next, La Terrasse, France
[2]Centre National d'Etudes Spatiales, Toulouse, France
[3]Ocean Data Lab, Plouzané, France
[4]Ifremer, Plouzané, France
[5]Collecte Localisation Satellite, Ramonville Saint Agne, France

Key Points:

- The Near Inertial Oscillations (NIOs) challenge the mapping of total surface current from future Spaceborne Doppler data and Altimetry.
- The challenge can be tackled with inversion schemes accounting for the coherency of NIOs, allowing inversion of the current components.
- Altimetry is an essential component to disentangle geostrophy from the other components of the total surface current.

Abstract

Two methods for the mapping of ocean surface currents from satellite measurements of sea level and future current vectors are presented and contrasted. Both methods rely on the linear and Gaussian analysis frameworkwith different levels of covariance definitions. The first method separately maps sea level and currents with single-scale covariance functions and leads to estimates of the geostrophic and ageostrophic circulations. The second maps both measurements simultaneously and projects the circulation onto 4 contributions: geostrophic, ageostrophic rotary, ageostrophic divergent and inertial. When compared to the first method, the second mapping moderately improves the resolution of geostrophic currents but significantly improves estimates of the ageostrophic circulation, in particular near-inertial oscillations. This method offers promising perspectives for reconstructions of the ocean surface circulation. Even the hourly dynamics can be reconstructed from measurements made locally every few days because nearby measurements are coherent enough to help fill the gaps. Based on numerical simulation of ocean surface currents, the proposed SKIM mission that combines a nadir altimeter and a Doppler scatterometer with a 300 km wide swath (with a mean revisit time of 3 days) would allow the reconstruction of 50% of the near-inertial variance around an 18 hour period of oscillation.

Plain Language Summary

Ocean surface currents are caused by a variety of phenomena that varies at different space and time scales. Here we mainly consider the two dominant contributions. The first is the current resulting from the quasi-equilibrium between the sloping sea level and the Coriolis force, slowly evolving over a few days. The second is also associated with the Coriolis force, but out of equilibrium: oscillating currents caused by rapid changes of the wind with a narrow range of periods around a natural period of oscillation that increase with latitude from 12 hours at the poles. For many applications it is desirable to separate these two contributions, for example to compute transports associated to the slowly evolving component and to evaluate the amount of kinetic energy pumped by the wind, mostly in the fast oscillations. This separation is easy with hourly sampled in situ measurements, but few are available. Here we show that we can perform this separation using satellite passes with measurements of sea level and a swath of surface current vectors, as can be measured by proposed future satellites. The fast oscillations can be reproduced even if data is available every few days, thanks to their spatial patterns and temporal coherence.

1 Introduction

The ocean surface current, a key variable for many scientific and operational applications, is only partially and indirectly observed from space. Altimetry provides the geostrophic component of the current (Fu et al., 1988), which is a dominant contribution to surface transport in most of the oceans, effectively resolving wavelengths larger than about 200 km wavelength (Ballarotta et al., 2019). The ageostrophic component, not synoptically observed yet, is locally sampled from drifting buoys (Elipot et al., 2016) or High Frequency Radars near the coasts (Kim et al., 2008). If model estimates for ageostrophic current are available, in particular for the low-frequency part (Rio et al., 2014) the uncertainties are still high. Filling this gap with satellite measurements of the total surface current is the topic of active research, with several emerging concepts of spaceborne Doppler radar for either 1 km resolution local studies such as SEASTAR (Gommenginger et al., 2019) or global mapping at 10 to 30 km resolution with SKIM (Ardhuin, Brandt, et al., 2019, using a 300 km wide swath), STREAM (a new proposal for ESA Earth Explorer 11, using a 900 km wide swath) or WaCM (Rodríguez et al., 2019, using a 1200 to 1800 km wide swath), see Ardhuin, Chapron, et al. (2019) for a review. Similarly to

HF radar, these latter would provide radial components for multiple azimuth angles, from which the two-dimensional current vector could be assessed.

As for any satellite observation of a geophysical variable evolving in time and space, an important question is the ability to map the field given the instrument spatial resolution and time revisits. Satellite altimetry offers a very interesting example. Altimeters measure the anomaly of the Sea Surface Height (SSH) that contains the signature of various processes in the ocean spanning over a wide range of scales, some at a much higher frequency than the typical 10-day revisits of the Jason satellite orbits for instance. In practice, barotropic tides and response to high frequency winds and pressure turned out to be well handled (Carrère and Lyard (2003), Gille and Hughes (2001)) either from independent or empirical models, allowing accurate reconstructions of the mesoscale eddy field and , when combined with the mean dynamic topography, derived geostrophic currents (Le Traon & Dibarboure, 2002) with limited aliasing contamination. The case of total surface current brings new challenges. One of them is related to the signature of Near Inertial Oscillations (NIOs) (D'Asaro, 1985) which translates a natural mode of resonance in the ocean that is excited by winds at the surface. NIOs surface current have average root mean square (RMS) magnitudes of 7-15 cm/s at mid and high latitudes (Elipot et al., 2010; Yu et al., 2019), often comparable to the magnitude of currents in mesoscale eddies. In spite of efforts to understand and model NIOs (Pollard and Millard (1970), D'Asaro (1985), Whitt and Thomas (2015)), the predictability of NIOs is not yet accurate. Interactions with mesoscale also affect NIO propagation and dispersion which complicates its modeling (Young & Jelloul, 1997).

Relying on independent models of the high-frequency surface current is therefore not yet guaranteed. Although Doppler radar concepts may allow shorter time revisits than altimetry thanks to relatively wide swaths (Rodriguez et al., 2018), they may not directly sample inertial periods, e.g. a 18 hours period at 40° of latitude requires a revisit time of 9 hours for which a swath wider than 2500 km is necessary, which does not appear feasible with a single satellite mission. Therefore the reconstruction of surface current in time and space from space-borne Doppler is a challenge.

The focus of this paper is to explore this reconstruction challenge in simulation, taking the practical example of the SKIM Doppler concept combined with altimetry, using basic and improved mapping methods accounting for the physical properties of NIOs. The skills of the reconstruction will be evaluated quantitatively for both geostrophic and ageostrophic components in the North Atlantic basin.

2 Reconstruction methods

2.1 Background on linear analysis

The different mapping approaches explored in this study are all derived from the linear and Gaussian mapping framework reviewed below . We assume a state to estimate, noted $\mathbf{x}$, and partial observations, noted $\mathbf{y}$, that can be related to the state with a linear operator $\mathbf{H}$ such as:

$$\mathbf{y} = \mathbf{H}\mathbf{x} + \epsilon \tag{1}$$

where ϵ is an independent signal (e.g. observation error) not related to the state. If we define $\mathbf{B}$ the covariance matrix of $\mathbf{x}$ and $\mathbf{R}$ the covariance matrix of ϵ, both variables being assumed Gaussian, then the linear estimate is written:

$$\mathbf{x^a} = \mathbf{B}\mathbf{H^T}(\mathbf{H}\mathbf{B}\mathbf{H^T} + \mathbf{R})^{-\mathbf{1}}\mathbf{y}. \tag{2}$$

This formulation, known as Optimal Interpolation, requires the inversion of a matrix of the same size as the observation vector $\mathbf{y}$. When the number of observations exceeds the size of the state to resolve, it can be interesting to use an equivalent formulation given by the Sherman-Morrison-Woodbury transformation, allowing an inversion in state space, with a matrix of the size of the state vector $\mathbf{x}$,

$$\mathbf{x^a} = (\mathbf{H^T R^{-1} H} + \mathbf{B^{-1}})^{-1} \mathbf{H^T R^{-1} y}. \tag{3}$$

This second formulation is particularly useful when considering transformed states expressed in orthogonal bases (see section 2.3.1 where $\mathbf{B}$ becomes diagonal and the whole system gets easier to invert). If we note $\mathbf{K}$ the linear operator such as $\mathbf{x^a} = \mathbf{Ky}$ from Eq. (2) or Eq.(3), the covariance matrix of analysis error is given by:

$$\mathbf{B^a} = (\mathbf{I} - \mathbf{KH})\mathbf{B} \tag{4}$$

This latter can be used to characterize the uncertainty of the solution.

2.2 Basic mappings

In the basic mapping approaches, we perform separate mappings of the SSH and total surface current involving simple covariance functions in the $\mathbf{B}$ matrix defined separately for each variable. Then the geostrophic component is given by the derivation of SSH maps and the ageostrophic component by subtraction of the geostrophic component to the total current.

2.2.1 For SSH: the standard Aviso/CMEMS mapping

To map the SSH, we first map the Sea Level Anomaly (SLA), defined in reference to the long-term mean. We followed, as in the standard Aviso/CMEMS mapping, a basic formulation derived from Eq.2. The observation vector $\mathbf{y}$ is the SLA observations, noted $\mathbf{h^o}$. The state vector $\mathbf{x}$ is the gridded SLA. The observation operator $\mathbf{H}$ (a tri-linear interpolator tranforming the gridded state SLA to equivalent along-track SLA) is not written explicitely: in practice, the matrices $\mathbf{BH^T}$ and $\mathbf{HBH^T}$, representing the covariance of the signal in the (grid,obs) and (obs, obs) spaces, are directly written with the analogical formula of the covariance model as described in (Pujol et al., 2016). The $\mathbf{R}$ matrix, for representativity and instrumental errors, is assumed diagonal. Since the covariance of SLA is assumed to vanish beyond a few hundreds of kilometers in space and beyond 10 to 20 days in time ((Le Traon & Dibarboure, 2002)), separate inversions are performed locally selecting observations over time and space windows adjusted to these values. In practice, the number of observations being limited to less than 1000, the inversion in observation space is computationally manageable. Details on the map production are given in (Pujol et al., 2016). From the SLA maps, the SSH maps are given with the addition of the long-term mean subtracted before the mapping.

2.2.2 For total surface current: a bi-variate weighted least square

The total surface current has different covariance structures than SSH, and does not benefit from the long history of developments with operational systems (at least when the measurements are scattered in space and azimuth angles as in the SKIM concept). As a first level processing, we therefore choose a basic filter, where eq.(3) is applied locally to solve for a single current vector $\mathbf{x} = [u, v]^T$ from the radial velocity observations nearby within a time-space radius. In this context, $\mathbf{B}$ can be considered as infinite, and eq. (3) reduces to the following bivariate least square formula:

$$[u, v]^T = (\mathbf{H^T R^{-1} H})^{-1} \mathbf{H^T R^{-1} u_r^o}, \tag{5}$$

where $\mathbf{u_r^o}$ are the radial velocity observations. The $\mathbf{R}$ matrix represents the covariances of $\mathbf{u_r^o}$ errors, namely the representativity error and Doppler measurement error, both assumed diagonal. Note that $\mathbf{R^{-1}}$ can also be called the weight matrix $\mathbf{W}$, the weights being the inverse of observation error variances (set to $0.2^2\ \ (\mathrm{m/s})^2$ for the problem considered in section 3, which is an optimal value also including representativity errors). These weights also take into account the time and space radius, set to 40 km and 10 days in section 3, with a Hamming window. Finally, the observation operator $\mathbf{H}$ can be written from the vector of $\mathbf{u_r^o}$ azimuth angles $\theta_1 ... \theta_p$ as follows ,

$$\mathbf{H} = \begin{bmatrix} \cos(\theta_1) & \sin(\theta_1) \\ \vdots & \vdots \\ \cos(\theta_p) & \sin(\theta_p) \end{bmatrix} \tag{6}$$

where p is the size of the observation vector. Since $\mathbf{B}$ tends to infinity, the covariances of analysis error $\mathbf{B^a}$ given by the limit of Eq. (4) are written as:

$$\mathbf{B^a} = \mathbf{H^T R^{-1} H}. \tag{7}$$

A geometrical illustration of the solution is shown in Figure 1, with the ellipses of the solution uncertainty given by the $\mathbf{B^a}$ matrix of size (2×2). Note that at least two ob-

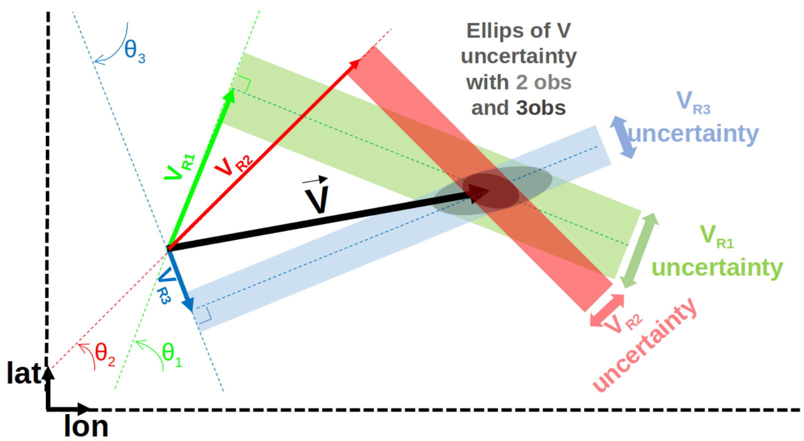

Figure 1: Scheme of the basic surface current mapping algorithm based on a bi-variate weighted least square, from at least two radial Doppler observations at different azimuth θ (here there are 3 observations V_{R1}, V_{R2}, V_{R3}).

servations at different θ angles are necessary to ensure invertibility of eq.(5), which is also illustrated on Figure 1. This is why the time-space radius must be carefully set with respect to the observation sampling.

2.2.3 Geostrophic and ageostrophic current gridded maps

The geostrophic current $(\mathbf{u_g}, \mathbf{v_g})$ is directly derived from the mapped SSH,

$$\begin{cases} u_g = -\frac{g}{f_c}\frac{\partial SSH}{\partial y} \\ v_g = \frac{g}{f_c}\frac{\partial SSH}{\partial x} \end{cases} \tag{8}$$

where f_c is the Coriolis frequency, which is a function of latitude. The ageostrophic estimates $(\mathbf{u_{ag}}, \mathbf{v_{ag}})$ are obtained by substraction to the total surface current $(\mathbf{u}, \mathbf{v})$ of section 2.2.2,

$$\begin{cases} u_{ag} = u - u_g \\ v_{ag} = v - v_g \end{cases} \tag{9}$$

These geostrophic and ageostrophic current estimates will be considered as the basic mapping solutions in section 4.

2.3 Improved mapping

The improved mapping also relies on linear analysis framework but with extended state, extended observation vector and multivariate covariances. For practical reasons, the inversion problem is framed in a reduced sub-component space such as to accommodate the number of observations in large spatio-temporal windows. This is particularly interesting to handle multiple signals of various scales in time and/or space.

2.3.1 Formulation

We consider an extended state vector $\mathbf{x}$ composed by N physical components (e.g. geostrophy, low and high frequency ageostrophy as proposed in section 2.3.2):

$$\mathbf{x} = (\mathbf{x_1^T}, ..., \mathbf{x_N^T})^\mathbf{T}. \tag{10}$$

Each component $\mathbf{x_k}$ contains the surface topography and surface current variables to be resolved in the grid space, noted $\mathbf{x_k} = (\mathbf{h_k^T}, \mathbf{u_k^T}, \mathbf{v_k^T})^\mathbf{T}$. The key aspect of the method is a rank reduction of the state vector, through a sub-component decomposition, such as $\mathbf{x_k}$ can be written as:

$$x_k = \begin{bmatrix} \Gamma_{k,h} \\ \Gamma_{k,u} \\ \Gamma_{k,v} \end{bmatrix} \eta_k = \Gamma_k \eta_k \tag{11}$$

where $\eta_\mathbf{k}$ is the reduced state vector for component k, $\mathbf{\Gamma_{k,h}}$, $\mathbf{\Gamma_{k,u}}$, and $\mathbf{\Gamma_{k,v}}$ are the sub-component matrices in topography and currents. Note that for some components, one of the block can be set to zeros (e.g. if ageostrophy component is considered with zero contribution on SSH). Their concatenation is called $\mathbf{\Gamma_k}$ which is the matrix transforming the reduced state vector in the grid space for topography and currents. In practice, $\mathbf{\Gamma_k}$ will be a wavelet decomposition of the time-space domain, with elements of appropriate temporal and spatial scales to represent the component k. These wavelet scales, and their specified variance set with a diagonal matrix noted $\mathbf{Q_k}$, will define the equivalent covariance model $\mathbf{B_k}$ in the grid space for component k:

$$\mathbf{B_k} = \mathbf{\Gamma_k Q_k \Gamma_k^T} \tag{12}$$

The observation vector $\mathbf{y}$ is also extended to the observed surface topography and surface current noted $\mathbf{y} = (\mathbf{h^{oT}}, \mathbf{u_r^{oT}})^\mathbf{T}$. Then, if $\mathbf{H_k}$ is the observation operator for component k (from grid space to observation space), we note $\mathbf{G_k} = \mathbf{H_k \Gamma_k}$ the sub-component matrix expressed in observation space. In these conditions, the observation vector $\mathbf{y}$ is the sum of all component contributions plus the unexplained signal ϵ (instrument error and representativity),

$$\mathbf{y} = \sum_{\mathbf{k=1}}^{\mathbf{N}} \mathbf{G_k} \eta_\mathbf{k} + \epsilon \tag{13}$$

If we use the notation $\eta = (\eta_\mathbf{1}^\mathbf{T}, ..., \eta_\mathbf{N}^\mathbf{T})^\mathbf{T}$ for the concatenation of the sub-component state vectors, and $\mathbf{G} = (\mathbf{G_1}, ..., \mathbf{G_N})$, then we have,

$$\mathbf{y} = \mathbf{G}\eta + \epsilon \tag{14}$$

Applying the same transformation from eq. (1) to eq. (3), to the reduced state vector η, the global solution is written:

$$\eta^{\mathbf{a}} = (\mathbf{G^T R^{-1} G} + \mathbf{Q^{-1}})^{-1} \mathbf{G^T R^{-1} y} \tag{15}$$

where $\mathbf{Q}$ is the covariance matrix of η, expressed as the concatenation of the diagonal matrices $\mathbf{Q_k}$ for each component. Finally the solution in the reduced-space projects into the grid space with the following relation:

$$\mathbf{x^a} = \mathbf{\Gamma} \eta^{\mathbf{a}} \tag{16}$$

In practice, in order to solve for Eq. (15), each block of $\mathbf{G}$ is directly filled from the analytical expression of the reduced-space elements (wavelets in section 2.3.2) constituting the columns of the matrix. Also, in many situations, the $(\mathbf{G^T R^{-1} G} + \mathbf{Q^{-1}})$ matrix, noted $\mathbf{A}$ hereafter, would be too large to be inverted (and even written) explicitly. We use a pre-conditionned conjugate gradient method to solve for $\eta = \mathbf{A^{-1} z}$ where $\mathbf{z} = \mathbf{G^T R^{-1} y}$ is a vector of reduced-state size computed initially from $\mathbf{G}$ and the observation vector $\mathbf{y}$. The algorithm involves many iterations of $\mathbf{A}\eta$ computations for updated η. Note that if $\mathbf{A}$ is too large to be written explicitly, the result $\mathbf{A}\eta$ can still be computed in two steps from a matrix multiplication of $\mathbf{G}$ then of $\mathbf{G^T}$. Once the convergence for the solution η is reached, the projection in physical grid space given by Eq. (16) is applied sequentially, by summing the analytical expression of the wavelets applied to grid coordinates (the columns of $\mathbf{\Gamma}$), separately for each component k.

As in any inversion based on linear analysis, the result strongly relies on the choice of covariance models, here defined by the reduced elements of each component. The choices of these elements are discussed in the following section.

2.3.2 Application to simultaneous mapping of geostrophy, low and high frequency ageostrophy

We propose to apply the above formulation for four components ($N = 4$), considering that the surface current is dominated by geostrophy, low frequency ageostrophy (splitting the low-frequency flow in rotationnal and divergent components for practical reasons) and high frequency ageostrophy, for which specific wavelet bases will be defined.

2.3.2.1 Geostrophy

Geostrophy is the component that has a signature on both topography and currents, where to expect some synergy between the altimetry and doppler observations. We define here the gridded variable $\mathbf{H_1}$ to resolve, and the corresponding gridded geostrophic current field $(\mathbf{U_1}, \mathbf{V_1})$ writes

$$\begin{cases} U_1 = -\frac{g}{f_c}\frac{\partial H_1}{\partial y} \\ V_1 = \frac{g}{f_c}\frac{\partial H_1}{\partial x} \end{cases} \tag{17}$$

The proposed reduced state for geostrophy is based on an element decomposition of $\mathbf{H_1}$, expressed by $\mathbf{\Gamma_{1,h}}$ with wavelets of various wavelength and temporal extensions. This will allow to approximate the standard covariance models used in altimetry mapping, accounting for specific variations with wavelength and time. A given p element of the decomposition $\mathbf{\Gamma_{1,h}}$ is expressed as follows:

$$\Gamma_{1,h}[i,p] = \cos(k_{x,p}(x_i - x_p) + k_{y,p}(y_i - y_p) + \Phi_p) * f_{\mathrm{tap}}(\frac{x_i - x_p}{L_{x_p}}, \frac{y_i - y_p}{L_{y_p}}, \frac{t_i - t_p}{L_{t_p}}) \tag{18}$$

where i is a given grid index of coordinates (x_i, y_i, t_i). For the ensemble of p, Φ_p is alternatively 0 and $\pi/2$, such as all subcomponents are defined by pairs of sine and cosine functions to allow the phase degree of freedom. $k_{x,p}$ and $k_{y,p}$ are zonal and meridional wavenumbers respectively, set to vary in the mappable mesoscale range (between 80km to 800km for the problem considered in section 3, with a spacing inversely proportional to the wavelet extensions, allowing to represent a signal of any intermediate wavelength). (x_p, y_p, t_p) are the coordinates of a space-time pavement. The function f_{tap} localizes the sub-component in time and space (at scales L_{t_p}, L_{x_p} and L_{y_p} respectively) as geostrophy has local extension of covariances. It is expressed as:

$$f_{\text{tap}}(\delta x, \delta y, \delta t) = \begin{cases} \cos(\pi\delta x/2) \times \cos(\pi\delta y/2) \times \cos(\pi\delta t/2), & \text{for} \quad (|\delta x|, |\delta y|, |\delta t|) < (1,1,1) \\ 0, & \text{elsewhere} \end{cases} \tag{19}$$

In practice, for the problem considered in section 3, L_{x_p} and L_{y_p} will be set to 1.5 the wavelength of element p and L_{t_p} to the decorrelation time scale of Aviso maps, on the order of 10 days in this region. Then, the same element p of the decomposition has also an expression in geostrophic current (through the geostrophic relation Eq. 8) written in the $\mathbf{\Gamma_{1,u}}$ and $\mathbf{\Gamma_{1,v}}$ matrices:

$$\begin{cases} \Gamma_{1,u}[i,p] = -g\,(\partial\Gamma_{1,h}[i,p]/\partial y_i)\,/f_c, \\ \Gamma_{1,v}[i,p] = g\,(\partial\Gamma_{1,h}[i,p]/\partial x_i)\,/f_c \end{cases} \tag{20}$$

As an illustration, $\Gamma_{1,h}[:,p]$ is shown on Figure 2 upper left panel, in plain color and $\Gamma_{1,u}[:,p]$, $\Gamma_{1,v}[:,p]$ in arrows. Here, this p^{th} component has a dominant wavelength $\lambda = \frac{2\pi}{\sqrt{k_{x,p}^2+k_{y,p}^2}}$ in a given direction. The lower-left panel represents the temporal extension of the sub-component set by L_{t_p}. The whole time-space domain is paved with similar

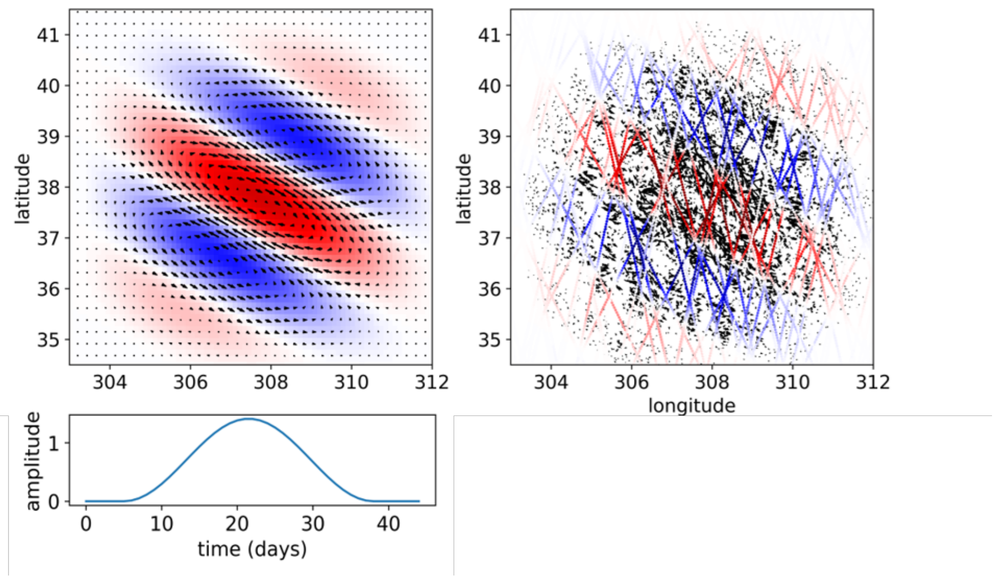

Figure 2: Illustration of a sub-component belonging to the mesoscale geostrophic component. The upper-left panel represents its expression in the grid space (= a column of the $\mathbf{\Gamma_1}$ matrix), in color for the topography ($\mathbf{\Gamma_{1_h}}$) and arrows for the current ($\mathbf{\Gamma_{1_u}}$ and $\mathbf{\Gamma_{1_v}}$), as a function of space. The lower-left panel represent the temporal modulation. The right panel represents the same sub-component in observation space considering altimetry tracks and scattered radial velocity observations at various azimuth angles, noted $\mathbf{G_1}$ declined in $\mathbf{G_{1_h}}$ (colors) and $\mathbf{G_{1_{u_r}}}$ (arrows).

sub-components, along coordinates (x_p, y_p, t_p) for wavelengths between 80km and 800km spanning in all directions of the plane. The ensemble can be seen as a wavelet basis. Finally, each sub-component p is assigned an expected variance in the $\mathbf{Q_1}$ matrix, consistent with the power spectrum observed from altimetry at the corresponding wavelength with isotropy assumption.

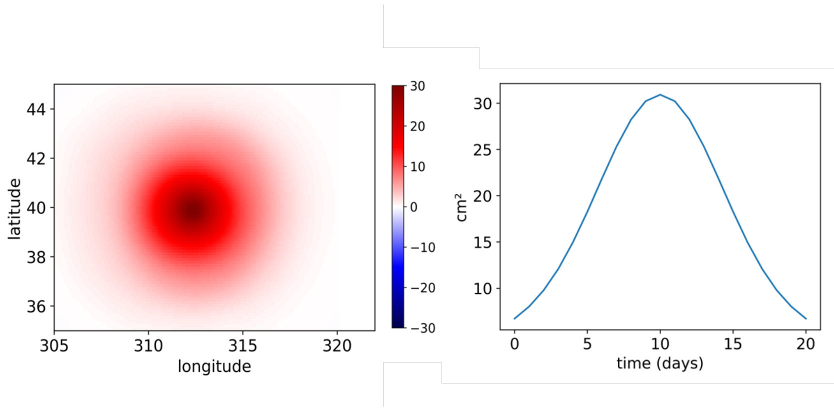

Figure 3: Illustration of the representor $\mathbf{\Gamma_{1_h}}[\mathbf{i},:]\mathbf{Q}\mathbf{\Gamma_{1_h}}$ for a given point i on the time-space grid (312°E,40°N, 10 days)represented as a function of space at 10 days (left panel) and as a function of time at 312°E,40°N.

For a given point i on the time-space grid (312°E,40°N, day 10), the representor $\mathbf{\Gamma_{1,h}}[\mathbf{i},:]\mathbf{Q}\mathbf{\Gamma_{1,h}}$ is plotted on Figure 3 , shown as a function of space (left panel) and as a function of time (right panel). It illustrates the equivalent covariance function, which is quite similar to what is currently used for altimetry mapping with OI inverted in observation space.

As mentioned in section 2.3.1, the inversion involves the construction of $\mathbf{G_1}$ matrix (see Eq.13), whose p^{th} column is represented on the right panel of Figure 2 considering altimetry tracks and scattered radial velocity observations at various azimuth angles described later in section 3. Here, the arrows are the projection of the $(\Gamma_{1_u}[:, p], \Gamma_{1_u}[:, p])$ along the various instrument azimuth angles and the colored dots the bilinear interpolation at nadir altimetry coordinates.

2.3.2.2 Low-frequency ageostrophy: rotational part

The low-frequency ageostrophy cannot be reduced a priori, as for geostrophy, to a single potential scalar field. However, if working with the zonal and meridional current $\mathbf{U}$ and $\mathbf{V}$ would be a first option to build the reduced state, we decided to work with the rotational and divergent current functions as they are scalars fields more likely to have isotropic features than the directional variables $\mathbf{U}$ and $\mathbf{V}$. Assuming isotropy of the scalar fields practically allows easier reduced space decomposition. This paragraph deals with the rotational flow, defined by a gridded variable $\mathbf{P}$ (potential) to resolve, such as the gridded SSH and surface current $(\mathbf{H_2}, \mathbf{U_2}, \mathbf{V_2})$ for this component are written:

$$\begin{cases} H_2 = 0 \\ U_2 = -\frac{\partial P}{\partial y} \\ V_2 = \frac{\partial P}{\partial x} \end{cases} \tag{21}$$

$\mathbf{H_2} = \mathbf{0}$ since we consider no contributions of $\mathbf{P}$ on SSH. A reduced state is considered for $\mathbf{P}$, constructed with single time/space window elements allowing the representation of the field down to a certain regularity in time and space. The proposed decomposition is much simpler than for topography, because the scales involved are larger in space and we did not find the necessity to tune the covariance model beyond to get acceptable results. The reduced state is represented in the time-space domain by the following $\mathbf{\Gamma_{2,P}}$ matrix:

$$\Gamma_{2,P}[i,p] = f_{\text{tap}}\left(\frac{x_i - x_p}{L_x}, \frac{y_i - y_p}{L_y}, \frac{t_i - t_p}{L_t}\right) \tag{22}$$

where f_{tap} is defined by Eq. 19. Here again, (x_p, y_p, t_p) are the coordinates to a space and time pavement. In practice, L_x, L_y and L_t correspond to the decorrelation scales (in time and space) of the reduced space. Using Eq 21, the matrices $\mathbf{\Gamma_{2,h}}$, $\mathbf{\Gamma_{2,u}}$ and $\mathbf{\Gamma_{2,v}}$ are written:

$$\begin{cases} \Gamma_{2,h}[i,p] = 0 \\ \Gamma_{2,u}[i,p] = -\frac{\partial \Gamma_{2,P}[i,p]}{\partial y_i} \\ \Gamma_{2,v}[i,p] = \frac{\partial \Gamma_{2,P}[i,p]}{\partial x_i} \end{cases} \tag{23}$$

As an illustration, the p^{th} column of $(\mathbf{\Gamma_{2,u}}, \mathbf{\Gamma_{2,v}})$ is represented on Figure 4. Here

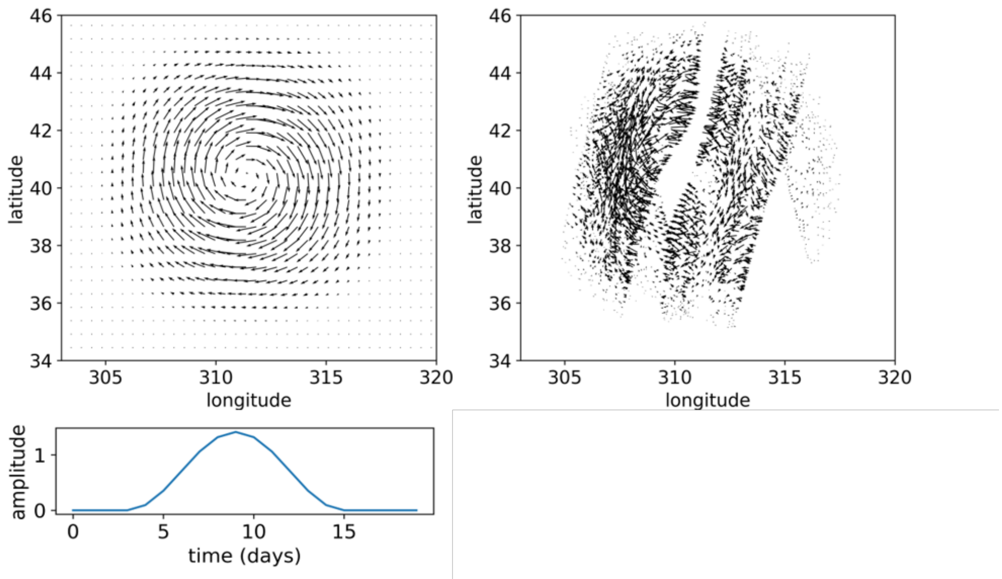

Figure 4: Illustration of a sub-component belonging to the low-frequency ageostrophic rotational component. The upper-left panel represents its expression in the grid space (= a column of the $\mathbf{\Gamma_2}$ matrix), the arrows for ($\mathbf{\Gamma_{2_u}}$ and $\mathbf{\Gamma_{2_v}}$), as a function of space. The lower-left panel represent the temporal modulation. The right panel represents the same sub-component in observation space , noted $\mathbf{G_{2,u_r}}$.

again, the whole time-space domain is paved with similar wavelet sub-components along coordinates $\mathbf{x_p}$, $\mathbf{y_p}$ and $\mathbf{t_p}$. The equivalent covariance model obtained from Eq.12, not shown, is overall similar to what is shown on Fig.2 for geostrophy, with a more basic spatial function only driven by L_x and L_y. It is set larger in space and shorter in time, aiming to capture large and more rapid signals than geostrophy. Targeting shorter scales in space would not be compatible with the observation dataset considered. In practice, for the problem considered in section 3, they will be set to 400km and 5 days in space and time, ensuring enough observations to resolve the total current at this space/time scale.

The p^{th} column of $\mathbf{G_2}$ matrix involved in the inversion is shown on the right panel of Figure 4 for illustration. It represents the projection of the sub-component vector field at the location and azimuth angle of all observations in the local domain.

2.3.2.3 Low-frequency ageostrophy: divergent part

The divergent part is handled exactly the same way as the rotational part, except that the gridded field to resolve is a Solenoidal function $\mathbf{S}$, such as the gridded SSH and currents $(\mathbf{H_3}, \mathbf{U_3}, \mathbf{V_3})$ for this component are written:

$$\begin{cases} H_3 = 0 \\ U_3 = -\frac{\partial S}{\partial x} \\ V_3 = -\frac{\partial S}{\partial y} \end{cases} \tag{24}$$

Here again, we consider no contributions of $\mathbf{S}$ on SSH. Following the same reduced-state decomposition for $\mathbf{S}$ than for $\mathbf{P}$, with a matrix noted $\mathbf{\Gamma_{3,S}}$, the matrices $\mathbf{\Gamma_{3,h}}$, $\mathbf{\Gamma_{3,u}}$ and $\mathbf{\Gamma_{3,v}}$ writes

$$\begin{cases} \Gamma_{3,h}[i,p] = 0 \\ \Gamma_{3,u}[i,p] = -\frac{\partial \Gamma_{3,S}[i,p]}{\partial x_i} \\ \Gamma_{3,u}[i,p] = -\frac{\partial \Gamma_{3,S}[i,p]}{\partial y_i} \end{cases} \tag{25}$$

The p^{th} column of $(\mathbf{\Gamma_{3,u}}, \mathbf{\Gamma_{3,v}})$ is represented on the left panel of Figure 5 for illustration, as well as the p^{th} column of the $\mathbf{G_2}$ matrix involved in the inversion.

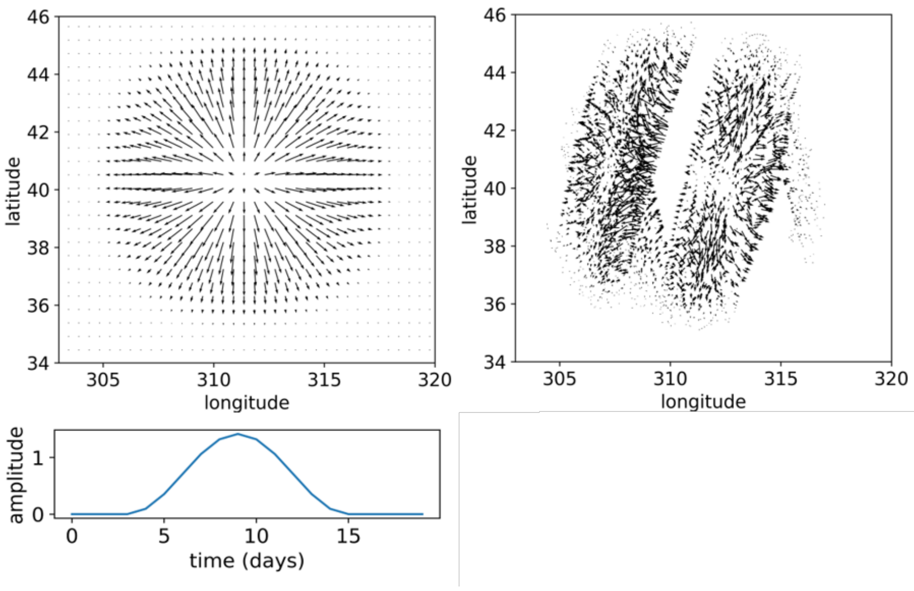

Figure 5: Illustration of a sub-component belonging to the low-frequency ageostrophic divergent component. The upper-left panel represents its expression in the grid space (= a column of the $\mathbf{\Gamma_3}$ matrix), the arrows for ($\mathbf{\Gamma_{3_u}}$ and $\mathbf{\Gamma_{3_v}}$), as a function of space. The lower-left panel represent the temporal modulation. The right panel represents the same sub-component in observation space, noted $\mathbf{G_{3_{u_r}}}$.

2.3.2.4 High-frequency ageostrophy (NIO)

This component stands for the near inertial motions featuring very distinct oscillating patterns near the inertia frequency f_c. It is possible to define a reduced space made of two gridded fields to resolve $\mathbf{A}$ and $\mathbf{B}$, slowly varying in time and space with the gridded SSH and current field (H_4, U_4, V_4) expressed as follows:

$$\begin{cases} H_4 = 0 \\ U_4 = A\cos(-2\pi f_c t) + B\sin(-2\pi f_c t) \\ V_4 = A\sin(-2\pi f_c t) - B\cos(-2\pi f_c t) \end{cases} \tag{26}$$

Here again, we assume no contribution on SSH. This current field oscillates near the inertia frequency, with a coherency related to the time variations of $\mathbf{A}$ and $\mathbf{B}$. Note that the distinct $\mathbf{A}$ and $\mathbf{B}$ allow the degree of freedom on the phase of the NIOs. The reduced space for $\mathbf{A}$ and $\mathbf{B}$ is defined by the following $\mathbf{\Gamma_{4_A}}$ and $\mathbf{\Gamma_{4_B}}$ identical matrices, giving:

$$\Gamma_{4,A}[i,p] = \Gamma_{4,B}[i,p] = e^{-\frac{|t_i - t_p|^q}{\tau^q}} f_{\text{tap}}(\frac{x_i - x_p}{L_x}, \frac{y_i - y_p}{L_y}, 0) \tag{27}$$

The time decay is not set with the f_{tap} function, but with an exponential of degree q which seemed to better represent actual time perturbations of the oscillations. For the problem considered in section 3, L_x and L_y will be both set to 250km, q at 2 and τ at 3 days. These values were optimized to fit the covariance properties of the NIOs signal in the reference simulation. Using Eq. (26), the matrices $\mathbf{\Gamma_{4,h}}$, $\mathbf{\Gamma_{4,u}}$ and $\mathbf{\Gamma_{4,v}}$ writes:

$$\begin{cases} \Gamma_{4,h}[i,p] = 0 \\ \Gamma_{4,u}[i,p] = \Gamma_{4,A}[i,p]\cos(-2\pi f_c t) + \Gamma_{4,B}[i,p]\sin(-2\pi f_c t_i) \\ \Gamma_{4,v}[i,p] = \Gamma_{4,A}[i,p]\sin(-2\pi f_c t) - \Gamma_{4,B}[i,p]\cos(-2\pi f_c t_i) \end{cases} \tag{28}$$

The p^{th} column of $(\mathbf{\Gamma_{4,u}}, \mathbf{\Gamma_{4,v}})$ is represented on the left panels of Figure 6 for illustration. The arrows on the upper panel indicate a spatially coherent pattern of NIOs, actually rotating in time as indicated by the time-modulation on the lower panel.

Finally, the p^{th} column of the $\mathbf{G_4}$ matrix involved in the inversion is shown on the right panel of Figure 6. The arrows indicate multiple directions are the observations span over different times in the local domain of the sub-component.

3 Observing System Simulation Experiments

3.1 The reference scene

Ocean circulation numerical models provide realistic scenes of ocean variability, useful to assess the impact of existing and future observing systems. In this study, we used the outputs of a high-resolution (1/60° in the horizontal) simulation at hourly frequency, the NEMO NATL60-CJM simulation further described in (Amores et al., 2018). This simulation, forced with hourly winds, allows the resolution of a wide spectrum of processes at ocean surface, from basin to sub-mesoscales and from annual to hourly scales including NIOs, in the North Atlantic region. This simulation does not include tidal forcing, but as discussed in the conclusion, this should not impact our analysis. The SSH and surface current in the first layer constitute our ground-truths in the experiments spanning over the year 2012.

3.2 Synthetic observations from instrument simulators

The instrument simulators are based on existing software used to generate synthetic observations. They perform a sampling, in time and space, of the reference scene over the satellite view along the orbit, and generate a realistic measurement error, either instrumental or geophysical.

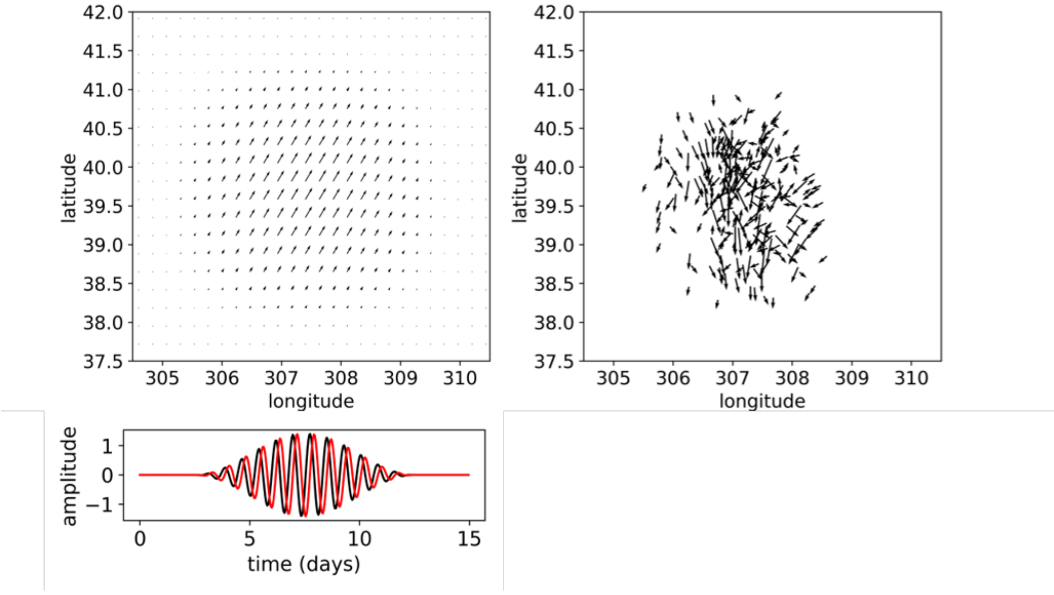

Figure 6: Illustration of a sub-component belonging to the high-frequency ageostrophic component. The upper-left panel represents its expression in the grid space (and corresponds to a column of the $\mathbf{\Gamma_4}$ matrix), the arrows for ($\mathbf{\Gamma_{4_u}}$ and $\mathbf{\Gamma_{4_v}}$), as a function of space. The lower-left panel represent the temporal modulation for the zonal u (black) and meridional v (red) components. The right panel represents the same sub-component in observation space, noted $\mathbf{G_{4_{u_r}}}$.

3.2.1 The altimetry simulator

The altimetry simulator (Gaultier et al., 2016) in its nadir version was used in this study to simulate a constellation of 5 altimeters on different orbits (two Jason-like and three Sentinel3-like). The model SSH was sampled at 1 Hz posting (approximately 6 km) along these orbit tracks over 1-year. An instrumental error of 3cm RMS at 1Hz was applied to all satellites following a random Gaussian law to simulate the white-noise plateau. An illustration of the altimetry dataset is shown on the top panels of Figure 7.

3.2.2 The Doppler simulator

The Doppler simulator for the SKIM concept, called 'SKIMulator' (Gaultier, 2019a, 2019b), was developed in the context of SKIM phase A studies by ESA (ESA, 2019). The simulator was applied on the first-layer vector current of the reference field, providing radial current vectors along multiple azimuth angles of the rotating beams as illustrated by the green arrows on Figure 8. An instrument error is applied, accounting for radar noise and Doppler processing errors such as the error in the surface wave Doppler retrieval, as further described in (F. Ardhuin et al., 2019).The total error is on the order of 5-10 cm/s. The overall swath, of 270km width, samples any given point of the Ocean at orbit repeat (12days), and according to the latitude, the ascending/descending and overlapping swaths allow several revisits at different intervals.

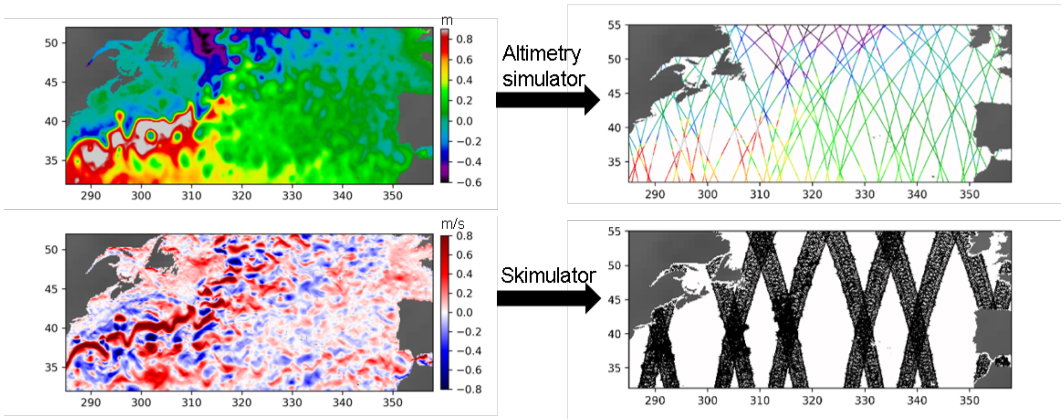

Figure 7: Schematic showing the instrument simulator sampling (altimetry on the top, doppler current Skimulator on the bottom) from the reference scene on the left to the sampled data with instrument error added on the right. Three-day worth of synthetic data are shown on the right panels.

4 Results

4.1 Reconstruction of Geostrophic and Ageostrophic current

The reconstructed geostrophic current (zonal and meridional) compares well with the reference (geostrophic component derived from the reference SSH) as suggested by Figure 9 for both basic and improved mapping. Minor differences appear with slightly finer structures in the second case with error fields slightly reduced (3rd versus 5th rows on the figure). This will be quantified in section 4.2

The left three panels of figure 10 shows the same snapshots (reference, basic and improved mapping) for the ageostrophic component. The reference ageostrophic field on the top is the reference total current minus the reference geostrophic current. Here, as opposed to geostrophy, the fields are fairly different. The temporal evolution of these fields is shown for a selected location on the right panel. First, we note the reference current is composed of periodic fluctuations of approximate near-inertial frequency on top of a slower signal. The spatial scales of the dominent patterns is larger than the mesoscale eddies, probably linked to the atmospheric wind field patterns. Estimated ageostrophic field with basic mapping clearly fails on several aspects. By construction, inertial motions are not resolved since they occur at a much higher frequency than the filtering scales of the basic mapping so the time series (blue line) does not feature oscillations. Furthermore, the low frequency component does not seem accurate. Given the small number of Doppler instrument revisits (as represented by the grey diamonds on the right panel) the estimation suffers from aliasing. For instance, between days 15 and 30, the observations happen to occur primarily near the maxima of the oscillations for the zonal component, leading to overestimation of the zonal component at low-frequency (blue curve) in this particular case. However, the estimated ageostrophic field with improved mapping is fairly different. It does resolve inertial motions, and succeeds in capturing, to a large extent, their modulation and phase. The reconstruction capability is based on the degrees of freedom of the signal with respect to the number of independent observations. Since the spatial patterns of our "true" NIOs are quite large and their temporal extension exceeds a few inertial periods, a large volume in time/space can be constrained with the Doppler observations. From the reconstructed series (red line on the right panel), it is also clear that the low frequency variations of the ageostrophy current is better resolved, the aliasing issue being now mitigated.

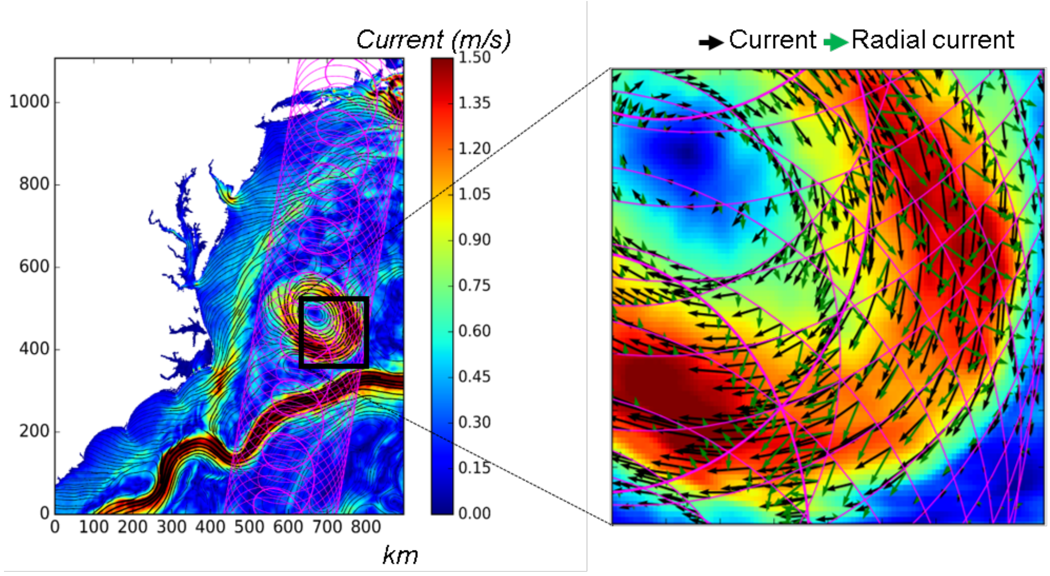

Figure 8: Detailed view of the SKIMulator outputs showing, with respect to the reference 2D current vectors in black, the observed radial current along the satellite azimuth angles in green.

We illustrate on Figure 11 the total current(represented by local Lagrangian trajectories) obtained with the two methods. The effect of resolving inertial motions clearly shows up on the Lagrangian trajectories, looping like actual drifter trajectories when the near inertial current amplitudes exceeds the low-frequency current.

4.2 Reconstruction skills as a function of spatial and temporal scales

We propose a quantitative analysis of the reconstructions, both in the spatial and temporal spectral domain. This will validate the results discussed above and further shed light on the reconstruction skills as a function of spatio-temporal scales. The analysis is based on the spectral ratio of the error over the true signal, computed along spatial or temporal sections of the domain. For spatial analysis, the computation is similar to what was proposed in (Ballarotta et al., 2019) to assess the effective resolution of Sea Level Anomaly products, but on the velocity in the normal direction of the section. For temporal analysis, the rotary spectra are considered for the spectral ratio, leading to two separate estimates in the clockwise and counter-clockwise directions. These ratios r are represented under the form of a percent scores $100*(1-r)$ summarized on Figures 12 and 13 for the different runs and components. As suggested by the upper panels of Figure 12, for geostrophic reconstructions, the improvements from basic mapping (green curves) to improved mapping (red curves) are sensible at all scales, especially below 150km. If we consider 50% as a reasonable threshold, then the resolving capabilities of the altimeter reconstruction for zonal and meridional current is about 110km, and 90km with SKIM combination. This is still a fair improvement for a single instrument added to an existing 5-instrument constellation. From this experiment, the Doppler observations would therefore improve the geostrophic component reconstruction even though altimetry is already efficient to capture this particular component. An additional experiment was led with improved mapping from Doppler observations only, represented in blue on the figure. The performances are not as good as with the combination, but do exceed those of

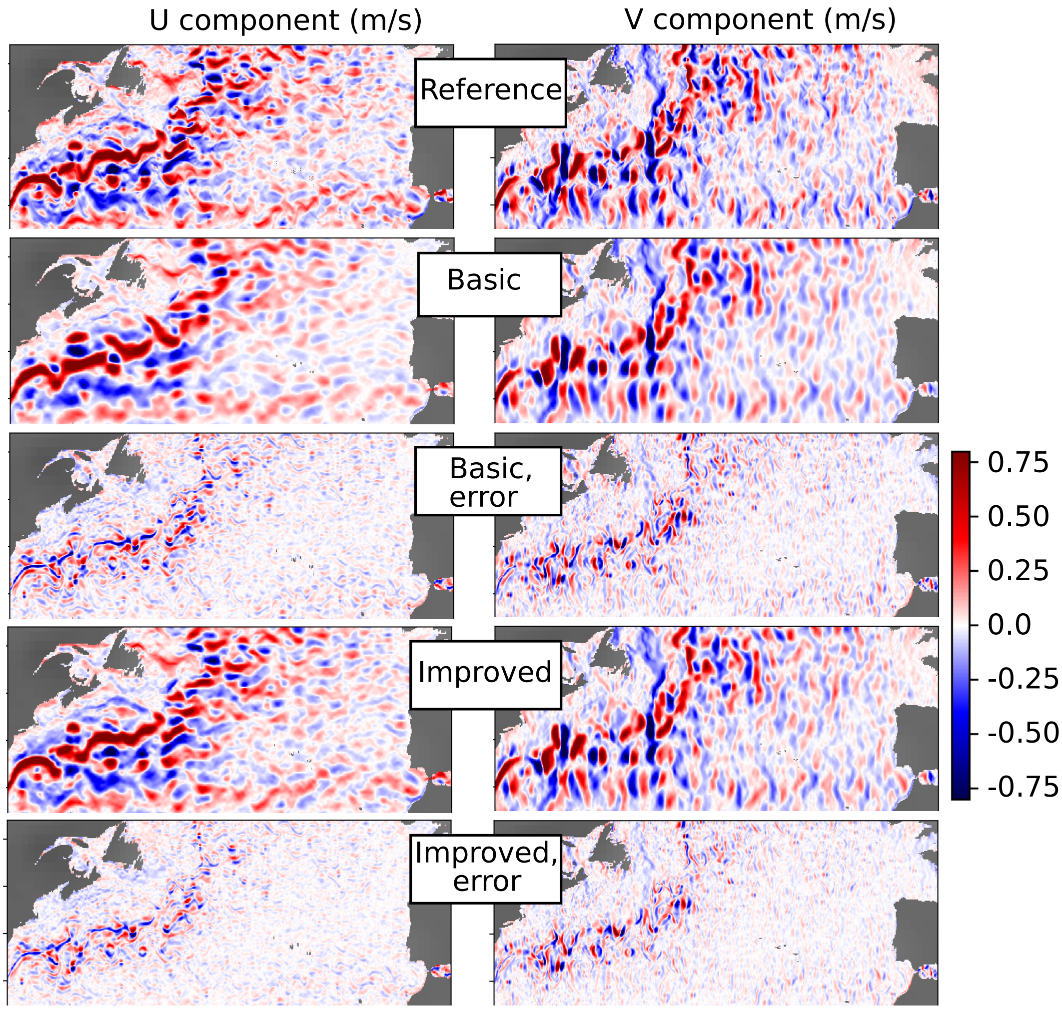

Figure 9: Snapshots of the geostrophic component (m/s) in the zonal (left column) and meridional (right column) directions, with differences (errors). The upper row is the reference, the second and third rows are the basic reconstructions and errors (w.r.t. reference) respectively. The fouth and fith rows are the same as second and third for the improved mapping.

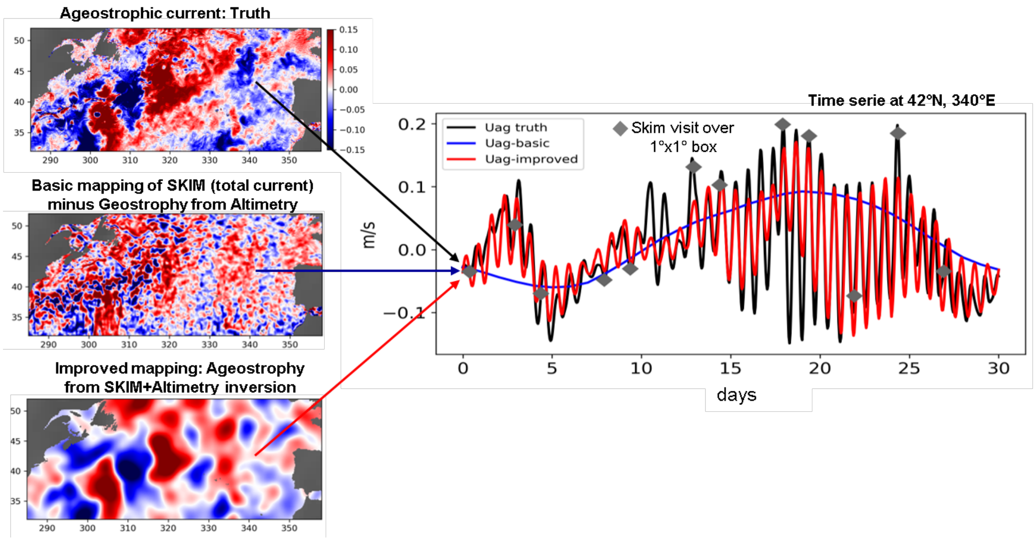

Figure 10: Reconstruction of the zonal ageostrophic component compared to the reference, in m/s. Upper left panel: snapshot of true (reference) ageostrophic zonal current. Middle left panel: reconstruction from basic mapping. Lower left panel: reconstruction from improved mapping. Right panel: time series of the reference (black), basic mapping (blue) and improved mapping (red) at 340°E, 42°N as a function of time over a month.

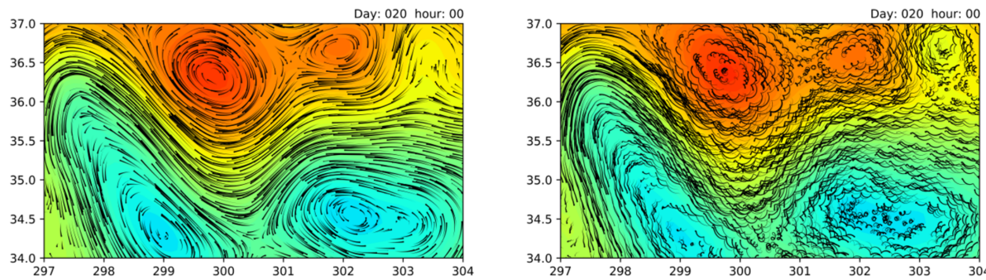

Figure 11: SSH (plain color) and local Lagrangian trajectories (black lines) of the surface current resolved with basic (left) and improved (right) mapping.

altimetry only at small scales (below 250km). At large scales, the ambiguity with ageostrophy, in absence of altimetry, certainly explains the lower performances.

We also note minor differences between the zonal and meridional performances: at large scales beyond 250km, the meridional component seems slightly better resolved with altimetry and SKIM, meaning that the zonal gradients of SSH would be more accurate at these large scales. With SKIM, the design was indeed found to perform better for along-track azimuth angles on swath average (Gaultier, 2019b) resulting in slighly better meridional currents on global average.

For ageostrophic reconstructions (lower panels of Figure 12), more sensitive differences were found as expected. Indeed, with the basic mapping, only the largest scales are partially resolved. Because of aliasing issues discussed in 4.1, the portion of resolved signal is weak, of about 15% (zonal) to 30% (meridional) beyond 1000km wavelength. However, the reconstruction with improved mapping exceeds 45% above 500km, where most of the inertial energy is. Note that, by construction of the sub-components for ageostrophic current, we do not aim to resolve scales below 300km. This could be explored, but doing so with this observing system would be a challenge because of high-temporal frequencies at short spatial scales. The dashed lines, showing the NIO contribution only, indeed suggest that most of the improvements owe to the inertial part. The experiment with Doppler observations only (blue curve) also brings interesting results. The drop in performances, especially at large scales, suggests the importance of an altimetry constellation the better separate the geostrophic contribution and therefore better estimate the ageostrophic component as well.

The score evaluations in the time-frequency domain (Figure 13) bring additional elements, in particular about the low-frequency ageostrophy, by comparing the plain (NIO+ low-frequency ageostrophy) with the dashed (NIO only) lines on the lower panels. The low-frequency ageostrophy is indeed an essential component, allowing a recontruction score above 50% to 60% beyond a week period. We also found (not shown) that the rotational part was dominent over the divergent part, which is not surprising since the low frequency wind should be directly related to low-frequency wind, mostly rotational. The inertial peak appears also clearly on the scores at around 16 hours in the clockwise direction (lower-left panel). For geostrophy (upper panels) the time window does not allow to fully resolve the eddy time band (mostly beyond a month) where scores would reach the values found in the spatial analysis. However, the relative scores are consistent, we note that the relative improvement between the two methods (green versus red) are high between 5 and 10 days, suggesting that the time aliasing mitigation is efficient. We also note no significant differences between clockwise and counter-clockwise directions, as expected since quasi-geostrophic motions have similar energy for the two components of their rotary spectra.

5 Conclusions and perspectives

This study demonstrated, in principle, the possibility to disentangle and map various components of the ocean surface current from partial observations of the surface dynamic topography and current. This was achieved thanks to a specific treatment of the covariance structures used in the mapping. Indeed, for mid-latitudes, the time revisits of proposed spaceborne instruments for surface current measurements exceeded half the inertial periods, where a large part of the signal energy is. Basic mapping algorithms, acting as a low-pass filter, not surprisingly fail in resolving those signals and also introduce strong aliasing. The improved mapping presented here performs well thanks to the spatial and temporal coherence of high-frequency signals, long enough with respect to observation sampling. However, several additional tests (not shown) also show that increasing the time sampling, with a wider swath such as proposed in the WaCM or STREAM design, or a constellation of several SKIM-like satellites can resolve a much larger fraction of the NIOs variance even if it comes with higher instrumental noise. The present work therefore should help in the identification of trade-offs for the optimization of Doppler scatterometer designs and orbit choice. In general altimetry is an essential source of observations in addition to Doppler scatterometers, in particular to disentangle the surface current components.

The results of the reconstruction method considered in this study probably depends on the basis of sub-components chosen. This latter have been constructed manually with a wavelet basis approach, accounting for coherent structures seen in the different component of the flow considered. This method has the limitation to project observations on prescribed bases, requiring a priori knowledge of the signal characteristics (**G** matrix) and statistics (**Q** matrix). Also, potential interactions between the components, for in-

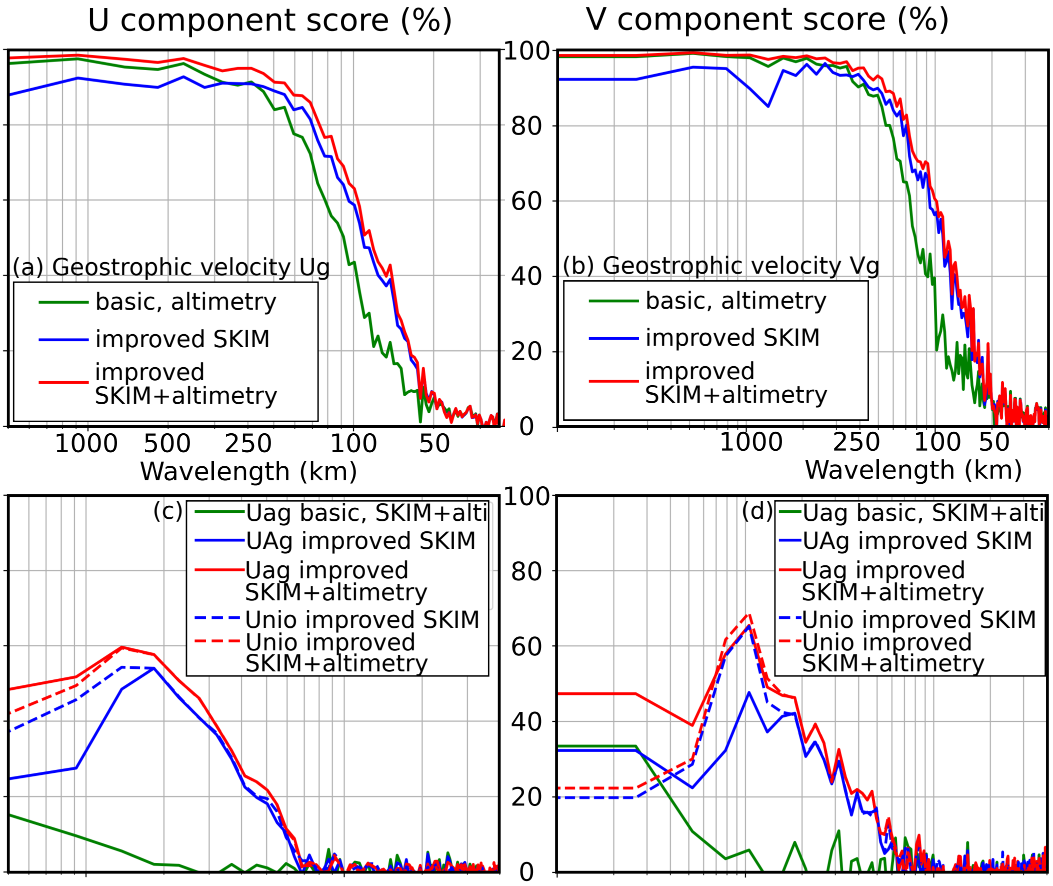

Figure 12: Performances as a function of spatial wavelength computed, in percent, from the ratio of the reconstruction error spectrum by the true signal spectrum. 100% means a full reconstruction with no errors.(a) Scores for geostrophic zonal current with basic mapping of altimetry (green), with improved mapping of SKIM (blue) and with improved mapping of SKIM + Altimetry combined (red).(b) same for meridional current. (c) scores for ageostrophic zonalcurrent with basic mapping of SKIM + Altimetry combined (green), with improved mapping of SKIM (blue) and with improved mapping of SKIM + Altimetry combined (red). The dashed lines represent the contribution of near-inertial current only. (d) same for meridional current.

stance the impact of mesoscale eddies on inertial oscillations through relative vorticity fluctuations, is not yet accounted. We also acknowledge that tidal currents have not been considered is this experiment as the reference run is tide-free. However, dedicated analyses presented in (F. e. a. Ardhuin, 2019) suggest that tidal current may be well handled thanks to accurate barotropic models and favorable orbit aliasing. Baroclinic tidal currents, not always phase locked (Zaron, 2019) may also be a challenge, but they are probably dominated by shorter scales with a minimal interaction with inertial oscillations.

The practical applicability of the present result strongly depends on the realism of the surface current field, in particular its ageostrophic component. A preliminary analysis of drifter pairs, which will be reported elsewhere, suggests that half of the velocity variance is contained in covariances with scales larger than 100 km (Xiaolong Yu, personal communication 2019). We thus expect that the present approach is qualitatively

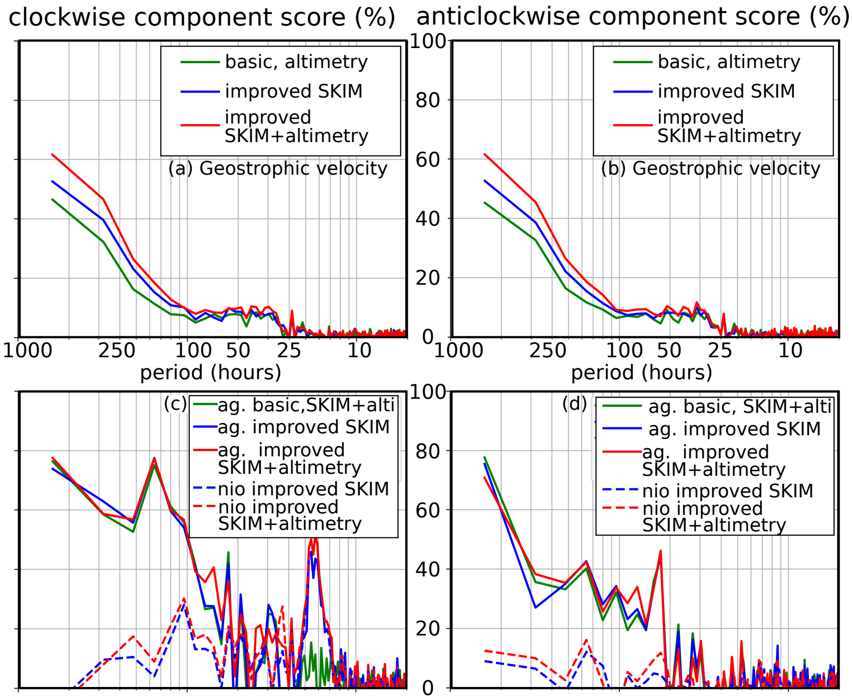

Figure 13: Performances as a function of temporal frequency computed, in percent, from the ratio of the reconstruction error rotary spectrum by the true signal error rotary spectrum. (a) Scores for geostrophic clockwise current with basic mapping of Altimetry (green), with improved mapping of SKIM (blue) and with improved mapping of SKIM + Altimetry combined (red). (b) same for counter-clockwise current. (c) scores for ageostrophic clockwise current with basic mapping of SKIM + Altimetry combined (green), with improved mapping of SKIM (blue) and with improved mapping of SKIM + Altimetry combined (red). The dashed lines represent the contribution of near-inertial current only. (d) same for counter-clockwise current.

valid, and that there may also be a chance to successfully invert some near inertial current from the drifters alone in regions of high drifter density like subtropical Gyres.

Acknowledgments

This study was funded by the Centre National d'Etudes Spatiales (CNES) as part as the SKIM phase A contract for the mapping algorithm developped in section 2.3 and by the European Space Agency (ESA) as part of the SKIM-SciSoc contract for the mapping algorithm implemented in section 2.2.

All data used in this study (reference fields, synthetic observations and gridded analysis) are available on the following repository: [ongoing, see 'materials for reviewers']

References

Amores, A., Jordà, G., Arsouze, T., & Le Sommer, J. (2018). Up to what extent can we characterize ocean eddies using present-day gridded altimetric products? *Journal of Geophysical Research: Oceans*, *123*(10), 7220-7236. Retrieved from `https://agupubs.onlinelibrary.wiley.com/doi/abs/10.1029/2018JC014140` doi: 10.1029/2018JC014140

Ardhuin, Brandt, P., Gaultier, L., Donlon, C., Battaglia, A., Boy, F., ... Stammer, D. (2019). Skim, a candidate satellite mission exploring global ocean currents and waves. *Frontiers in Marine Science*, *6*, 209. Retrieved from https://www.frontiersin.org/article/10.3389/fmars.2019.00209 doi: 10.3389/fmars.2019.00209

Ardhuin, Chapron, B., Maes, C., Romeiser, R., Gommenginger, C., Cravatte, S., ... Bourassa, M. (2019). Satellite doppler observations for the motions of the oceans. , *100*. doi: 10.1175/BAMS-D-19-0039.1

Ardhuin, F., Chapron, B., Marié, L., Gressani, V., Nouguier, F., Delouis, J.-M., & Peureux, C. (2019, 05). *Estimation of non-geophysical doppler and wave doppler, and inversion algorithm for skim.* doi: 10.13140/RG.2.2.22907.98081/3

Ardhuin, F. e. a. (2019, 05). *Earth explorer 9 candidate mission skim –report for mission selection.*

Ballarotta, M., Ubelmann, C., Pujol, M.-I., Taburet, G., Fournier, F., Legeais, J.-F., ... Picot, N. (2019). On the resolutions of ocean altimetry maps. *Ocean Science Discussions*, *2019*, 1–27. Retrieved from https://www.ocean-sci-discuss.net/os-2018-156/ doi: 10.5194/os-2018-156

Carrère, L., & Lyard, F. (2003). Modeling the barotropic response of the global ocean to atmospheric wind and pressure forcing - comparisons with observations. *Geophysical Research Letters*, *30*(6). Retrieved from https://agupubs.onlinelibrary.wiley.com/doi/abs/10.1029/2002GL016473 doi: 10.1029/2002GL016473

D'Asaro, E. A. (1985). The energy flux from the wind to near-inertial motions in the surface mixed layer. *Journal of Physical Oceanography*, *15*(8), 1043-1059. Retrieved from https://doi.org/10.1175/1520-0485(1985)015<1043:TEFFTW>2.0.CO;2 doi: 10.1175/1520-0485(1985)015⟨1043:TEFFTW⟩2.0.CO;2

Elipot, S., Lumpkin, R., Perez, R. C., Lilly, J. M., Early, J. J., & Sykulski, A. M. (2016). A global surface drifter data set at hourly resolution. *Journal of Geophysical Research: Oceans*, *121*(5), 2937–2966. Retrieved from http://dx.doi.org/10.1002/2016JC011716 doi: 10.1002/2016JC011716

Elipot, S., Lumpkin, R., & Prieto, G. (2010). Modification of inertial oscillations by the mesoscale eddy field. *Journal of Geophysical Research: Oceans*, *115*(C9). Retrieved from https://agupubs.onlinelibrary.wiley.com/doi/abs/10.1029/2009JC005679 doi: 10.1029/2009JC005679

ESA. (2019, May). *Report for mission selection: SKIM* (Tech. Rep. No. ESA-EOPSM-SKIM-RP-3550). European Space Agency, Noordwijk, The Netherlands. doi: 10.13140/RG.2.2.22907.98081/3

Fu, L.-L., Chelton, D. B., & Zlotnicki, V. (1988, November). Satellite altimetry: Observing ocean variability from space. *Oceanography*, *1*. Retrieved from https://doi.org/10.5670/oceanog.1988.01

Gaultier, L. (2019a). *Skimulator repository.* https://github.com/oceandatalab/skimulator. GitHub.

Gaultier, L. (2019b). Skimulator user manual [Computer software manual]. Retrieved from https://github.com/oceandatalab/skimulator/blob/master/doc/source/science.rst

Gaultier, L., Ubelmann, C., & Fu, L.-L. (2016). The challenge of using future swot data for oceanic field reconstruction. *Journal of Atmospheric and Oceanic Technology*, *33*(1), 119-126. Retrieved from https://doi.org/10.1175/JTECH-D-15-0160.1 doi: 10.1175/JTECH-D-15-0160.1

Gille, S. T., & Hughes, C. W. (2001). Aliasing of high-frequency variability by altimetry: Evaluation from bottom pressure recorders. *Geophysical Research Letters*, *28*(9), 1755-1758. Retrieved from https://agupubs.onlinelibrary.wiley.com/doi/abs/10.1029/2000GL012244 doi: 10.1029/2000GL012244

Gommenginger, C., Chapron, B., Hogg, A., Buckingham, C., Fox-Kemper, B., Eriksson, L., . . . Burbidge, G. (2019). Seastar: A mission to study ocean submesoscale dynamics and small-scale atmosphere-ocean processes in coastal, shelf and polar seas. *Frontiers in Marine Science*, *6*, 457. Retrieved from https://www.frontiersin.org/article/10.3389/fmars.2019.00457 doi: 10.3389/fmars.2019.00457

Kim, S. Y., Terrill, E. J., & Cornuelle, B. D. (2008). Mapping surface currents from hf radar radial velocity measurements using optimal interpolation. *Journal of Geophysical Research: Oceans*, *113*(C10). Retrieved from https://agupubs.onlinelibrary.wiley.com/doi/abs/10.1029/2007JC004244 doi: 10.1029/2007JC004244

Le Traon, P. Y. L., & Dibarboure, G. (2002). Velocity mapping capabilities of present and future altimeter missions: The role of high-frequency signals. *Journal of Atmospheric and Oceanic Technology*, *19*(12), 2077-2087. Retrieved from https://doi.org/10.1175/1520-0426(2002)019<2077:VMCOPA>2.0.CO;2 doi: 10.1175/1520-0426(2002)019⟨2077:VMCOPA⟩2.0.CO;2

Pollard, R., & Millard, R. (1970). Comparison between observed and simulated wind-generated inertial oscillations. *Deep Sea Research and Oceanographic Abstracts*, *17*(4), 813 - 821. Retrieved from http://www.sciencedirect.com/science/article/pii/0011747170900434 doi: https://doi.org/10.1016/0011-7471(70)90043-4

Pujol, M.-I., Faugère, Y., Taburet, G., Dupuy, S., Pelloquin, C., Ablain, M., & Picot, N. (2016). Duacs dt2014: the new multi-mission altimeter data set reprocessed over 20 years. *Ocean Science*, *12*(5), 1067–1090. Retrieved from https://www.ocean-sci.net/12/1067/2016/ doi: 10.5194/os-12-1067-2016

Rio, M.-H., Mulet, S., & Picot, N. (2014). Beyond goce for the ocean circulation estimate: Synergetic use of altimetry, gravimetry, and in situ data provides new insight into geostrophic and ekman currents. *Geophysical Research Letters*, *41*(24), 8918-8925. Retrieved from https://agupubs.onlinelibrary.wiley.com/doi/abs/10.1002/2014GL061773 doi: 10.1002/2014GL061773

Rodriguez, E., Wineteer, A., Perkovic-Martin, D., Gál, T., W. Stiles, B., Niamsuwan, N., & Rodriguez Monje, R. (2018, 04). Estimating ocean vector winds and currents using a ka-band pencil-beam doppler scatterometer. *Remote Sensing*, *10*, 576. doi: 10.3390/rs10040576

Rodríguez, E., Bourassa, M., Chelton, D., Farrar, J. T., Long, D., Perkovic-Martin, D., & Samelson, R. (2019). The winds and currents mission concept. *Frontiers in Marine Science*, *6*, 438. Retrieved from https://www.frontiersin.org/article/10.3389/fmars.2019.00438 doi: 10.3389/fmars.2019.00438

Whitt, D. B., & Thomas, L. N. (2015). Resonant generation and energetics of wind-forced near-inertial motions in a geostrophic flow. *Journal of Physical Oceanography*, *45*(1), 181–208.

Young, W., & Jelloul, M. B. (1997). Propagation of near-inertial oscillations through a geostrophic flow. *Journal of marine research*, *55*(4), 735–766.

Yu, X., Ponte, A. L., Elipot, S., Menemenlis, D., Zaron, E. D., & Abernathey, R. (2019). Surface kinetic energy distributions in the global oceans from a high-resolution numerical model and surface drifter observations. *Geophysical Research Letters*, *46*, 9757–9766. doi: 10.1029/2019gl083074

Zaron, E. (2019, 05). Predictability of non-phase-locked baroclinic tides in the caribbean sea. *Ocean Science Discussions*, 1-23. doi: 10.5194/os-2019-53